Electrochemical Deposition of Biferrocene Derivative-Attached Gold Nanoparticles and the Morphology of the Formed Film

Mami Yamada, Tamon Tadera, Kenya Kubo, and Hiroshi Nishihara*

Department of Chemistry, School of Science, The University of Tokyo, Tokyo, Japan 113-0033

Received: September 27, 2002

The electrodeposition phenomenon of octyl thiolate-stabilized gold nanoparticles with a 2.3 ± 0.5 nm core diameter modified with biferrocene-terminated alkanethiolates on their surface (Au_n−BFc) has been investigated using cyclic voltammetry, STM and AFM morphological observation, and electrochemical quartz crystal microbalance (EQCM) of the deposited Au_n−BFc film. Consecutive potential scans causing two-step one-electron oxidation of the biferrocene units of Au_n−BFc in CH_2Cl_2 electrolyte solution produce the adhesive Au_n−BFc film on electrode surface. The deposition rate is lower for the biferrocene derivative on one particle θ_{BFc} with a smaller modification number and a kind of electrolyte anion: $ClO_4^- \sim BF_4^- \gg PF_6^-$. The STM and AFM images have revealed that the thickness of the Au_n−BFc film grows gradually by increasing the number of cyclic scans, forming many monolayer-level domains with ca. 80 nm diameter of the assembled Au_n−BFcs. The average interparticle spacing of neighboring Au_n−BFcs in the film is 7.5 nm, which is longer than the estimated diameter of whole Au_n−BFc species (5.9 nm). Analysis of boron in the film electrodeposited in Bu_4NBF_4−CH_2Cl_2 by the prompt γ-ray neutron activation (PGA) method shows that the BF_4^- ion is incorporated in the film. EQCM measurement suggests that not only ions but also the included CH_2Cl_2 solvent molecules in the film are moved in and out reversibly in a potential range of $E^{0\prime}{}_2$ of Au_n−BFc. These results indicate that the formation of ionic lattice including Au_n−BFc^{2+} and counterion is accompanied by the exclusion of CH_2Cl_2 solvent molecules among the particles in the initial deposition process.

Introduction

Recently, preparation methods of stable and size-controlled gold nanoparticles using alkanethiols have been developed,[1] and their special electronic and electrochemical properties[2] have been revealed. One important area of study on nanoparticles is the fabrication of their dimension-controlled assembly for the purpose of making new electronic and optical devices such as quantum wire,[3] single electron device,[4] and nonlinear optical films.[5] Several methods to induce assembly such as self-assembly using monodispersed particles;[6] chemical interaction using dithiol,[7] ionic polymers,[8] metal ions,[9] and organic ligands with an adsorptive group (including DNA);[10] or physical perturbation by electric field[11] or light[12] have been reported.

We recently reported a novel electrochemical procedure to fabricate redox-active Au[13] and Pd[14] nanoparticle films on electrode substrates using biferrocene (BFc) derivative-attached metal nanoparticles, Au_n−BFc, prepared by a substitution reaction[15] of octyl thiolate-covered metal nanoparticles (Au_n−OT) with the biferrocene-terminated alkanethiol derivative (BFcS). The electrodeposition is achieved by the two-electron oxidation of the BFc units attached to metal nanoparticles. We also found that the electroreductive deposition of Au nanoparticles was modified with the use of an anthraquinone derivative.[2h,16] This method can be utilized for constructing heterolayers of metal nanoparticles,[16a] and the film thus formed shows novel photoelectrochemical characteristics different from those of a single particle.

From these previous results, the metal nanoparticles functionalized with "multiredox" molecules can be generally aggregated on the electrode by electrooxidative or reductive reaction. Note that while the properties of ferrocenylalkanethiol-attached nanoparticles have been investigated,[17] there is no report on the deposition phenomenon by oxidation of redox sites on the surface. Thus, the detailed elucidation of the mechanism itself is of considerable interest, and can contribute to the advanced practical application of fabricated and more ordered metal nanoparticle assemblies, which may be used in conjunction with recent developments in the like-charge attraction in metastable colloidal crystallites.[18] Possible candidates for the driving force of this electrochemical aggregation are "physical interaction" and/or "chemical bond formation" among the particles (Figure 1). The former would be attributed to the collective interaction among the charged Au_n−BFc, electrolyte, and solvent in solution, while the latter could be defined as the coupling reaction of the BFc units on the neighboring nanoparticles, which could occur when they are oxidized to become reactive.[19]

The purpose of the present study is to evaluate the electrodeposition process noted above on the basis of electrochemical and spectroscopic measurements. We measured the electrodeposition rate and observed the surface structure of the Au_n−BFc films in STM and AFM images by varying several parameters of the deposition conditions in CH_2Cl_2 solutions of Au_n−BFc. The parameters were (i) electrolyte anion, (ii) the number of potential scans, and (iii) the modification number of BFc units on a nanoparticle surface (θ_{BFc}).

Experimental Section

Chemicals. All solvents and reagents used for syntheses were of extrapure grade, and were purchased from Kanto Chemicals

* To whom correspondence should be addressed. E-mail: nisihara@chem.s.u-tokyo.ac.jp. Fax and phone: +81-3-5841-4348.

10.1021/jp027086y CCC: $25.00
Published on Web 03/29/2003

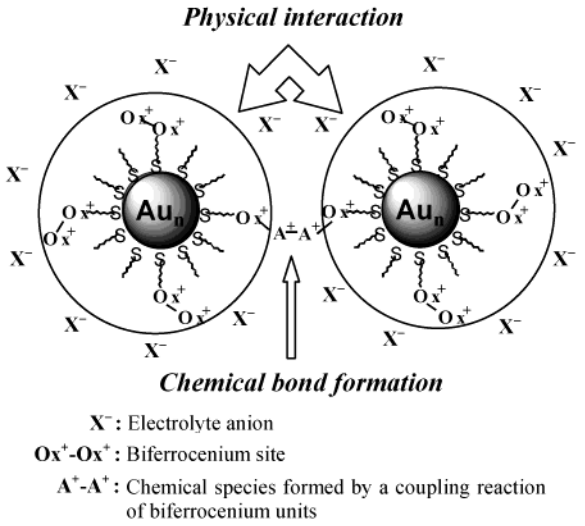

Figure 1. Two possible machanisms of electrodeposition between adjacent Au_n−BFc particles by electrooxidation.

or Tokyo Kasei. They were used as received, unless otherwise noted. Dichloromethane used for electrochemical measurements was of HPLC grade (Kanto Chemicals). Tetrabutylammonium salts, Bu_4NClO_4, Bu_4NBF_4, and Bu_4NPF_6 (HPLC grade, Kanto Chemicals) were used after recrystallization from ethanol.

Synthesis of 1-(9-Thiononyl-1-one)-1′,1″-biferrocene (BFcS). The synthetic procedure was based on that outlined in the previous literature.[13,20] The compound 1-(9-bromo-1-one)-1′,1″-biferrocene (758 mg, 1.32 mmol) was prepared with a yield of 45.4% by the Friedel−Crafts reaction of 1,1″-biferrocene with 8-bromooctyl chloride and aluminum chloride in CH_2Cl_2 at room temperature for 20 h, followed by the addition of thiourea (101 mg, 1.33 mmol) in ethanol (90 mL) and stirring at reflux for 40 h. The reaction mixture was basified with degassed 0.02 M aqueous NaOH (128 mL) by refluxing for 8 h to give a dark red oil in solution. After the solvent was evaporated in a vacuum, the residue was dissolved in $CHCl_3$ and filtered. The filtrate was dried over Na_2SO_4. The solvent was again evaporated in a vacuum, and the resulting red oil was chromatographed on silica gel using CH_2Cl_2. The fraction containing thiol ($R_f = 0.47$) was collected to give dark orange oil (502 mg, yield: 72%). Anal. Found: C, 62.4; H, 6.25; S, 5.83. Calcd for $C_{28}H_{32}OSFe_2 \cdot 0.5H_2O$: C, 62.6; H, 6.19; S, 5.97. IR (KBr) ν_{max}/cm^{-1}: 2568 (S−H), 1658 (C═O). UV−vis (CH_2Cl_2): λ_{max}/nm: 462. ^1H NMR ($CDCl_3$, 270 MHz) δ/ppm: 0.88 (t, 1H, $J = 7.4$ Hz), 1.20−1.70 (m, 10H), 2.42 (t, 2H, $J = 7.3$ Hz,), 2.51 (t, 2H, $J = 6.8$ Hz), 3.95 (s, 5H), 4.18 (t, 4H, $J = 1.6$ Hz), 4.28 (t, 2H, $J = 1.9$ Hz), 4.32 (t, 4H, $J = 1.6$ Hz), 4.55 (t, 2H, $J = 1.9$ Hz).

Synthesis of Octyl Thiolate-Covered Au Nanoparticle (Au_n−OT). The synthesis followed a standard procedure.[1a] In short, to a vigorously stirred solution of tetra-*n*-octylammonium bromide (4.58 g, 8.38 mmol) in 200 cm^3 of toluene was added $HAuCl_4 \cdot H_2O$ (0.776 g, 1.87 mmol) in 60 mL of deionized water stirred for 1 h. Octanethiol (0.274 g, 1.87 mmol) was added, then 0.5 M aqueous $NaBH_4$ (32 mL) was quickly poured into the vigorously stirred mixture. After the mixture was stirred for 3.5 h, the organic phase was separated, and the volume was reduced to ca. 10 mL with a rotary evaporator below 50 °C. The solution was suspended in 650 mL of ethanol and kept at −17 °C in a refrigerator for 12 h. The precipitates were collected by filtration on a membrane filter, and washed thoroughly with ethanol and acetone (330 mg, yield: 91.3%).

Synthesis of BFc-Attached Au Nanoparticle (Au_n−BFc). The modification of BFc units on the particle surface was

SCHEME 1: Preparation and Electrodeposition of Au_n−BFcs.

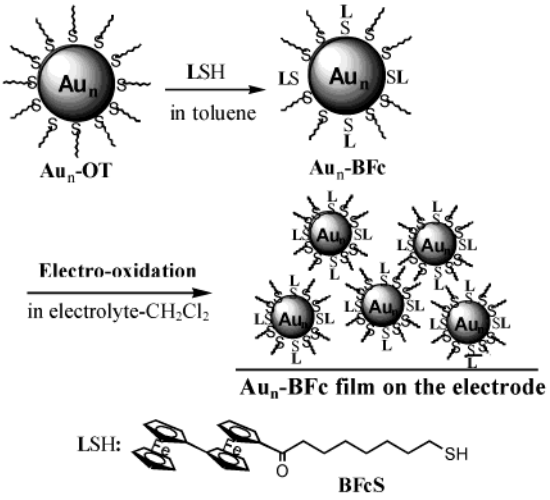

performed by a typical substitution reaction[15] of BFcS with Au_n−OT in toluene at room temperature (Scheme 1). The reaction conditions were conducted using the following solutions: (i) 25 mg/2 mL Au_n−OT solution for 24 h, (ii) 25 mg/12 mL Au_n−OT solution for 48 h, and (iii) 25 mg/2 mL Au_n−OT solution for 48 h. After addition of ethanol, the sample precipitated was collected by filtration and rinsed with ethanol and acetone to remove excess BFcS and displaced octanethiol. No contamination of free BFcS in the product was confirmed by ^1H NMR.

Spectroscopy. The ^1H NMR spectra of the samples in $CDCl_3$ were collected with a JEOL EX270 spectrometer. Infrared absorbance spectra were acquired using a JASCO FT/IR-620V spectrometer. UV−vis absorption spectra were recorded with an Agilent 453 UV−vis spectroscopy system. Inductively coupled plasma (ICP) measurements were carried out with a SII SPS-7000A spectrometer. The concentration of gold in the sample solution was calculated by a working curve using the standard reference material of gold at 242.795 nm.

The Prompt γ-ray Neutron Activation Analysis (PGA) Method.[21,22] Boron content of the film was assayed by the PGA method. The Au_n−BFc film employed for the analysis was prepared in a solution of 15 μM Au_n−BFc ($\theta_{BFc} = 7.5$) at HOPG in Bu_4NBF_4−CH_2Cl_2 with 120 potential scans. The surface of the film-deposited HOPG was thoroughly rinsed with CH_2Cl_2. The 478 keV γ-ray emitted from ^7Li produced via the $^{10}B(n,\alpha)^7Li$ reaction was used as the analysis line. Without any preprocessing, a film on the HOPG substrate was placed at the target position of the PGA system of the neutron beam guide at the JRR-3M reactor in Japan Atomic Energy Research Institute. An HOPG substrate without film was also examined for the purpose of checking the boron content. Aqueous solution of boric acid of exactly known amount was dropped on a piece of filter paper and dried to use as a boron standard. The prompt γ-ray spectrum of each sample was measured for 5000s by using a cold neutron beam with a flux of ca. 2×10^7 cm^{-2} s^{-1}. A special curve-fitting code[23] was employed in order to estimate the 478 keV peak areas because general curve-fitting programs are useless for analyzing the significantly Doppler-broadened peaks.[20]

Cyclic Voltammetry. Cyclic voltammetry was carried out in a standard one-compartment cell under an argon atmosphere at 25 °C using a platinum-wire counter electrode and an Ag/Ag^+ reference electrode [10 mM $AgClO_4$ in 0.1 M

Bu_4NClO_4−MeCN, $E^{0\prime}$ (Fc/Fc$^+$) = 0.27 V vs Ag/Ag$^+$ (Fc: ferrocene)] with a BAS CV-50W voltammetric analyzer. Electrodeposition of Au_n−BFc on an indium−tin oxide (ITO)-coated glass electrode (1.0 × 1.5 cm^2) or on a highly ordered pyrolytic graphite (HOPG: 0.28 mm^2) was carried out with consecutive scans between −0.3 and 0.9 V vs Ag/Ag$^+$ in a solution of Au_n−BFc in 0.1 M electrolyte (Bu_4NClO_4−CH_2Cl_2, Bu_4NBF_4−CH_2Cl_2, or Bu_4NPF_6−CH_2Cl_2). The ITO electrodes were washed in ultrapure water (>18.2 MΩ cm^{-1}) containing a protein remover for 5 min and cleaned sufficiently by ultrapure water and acetone for 5 min, respectively, under sonication before the experiment. The electrodeposited films were cleaned with CH_2Cl_2 after the preparation process then dried under vacuum.

Electrochemical Quartz Crystal Microbalance (EQCM) Measurement. EQCM was carried out in a standard Teflon cell under an argon atmosphere at 25 °C using a platinum-wire counter electrode and an Ag/Ag$^+$ reference electrode with a Hokuto HQ-101B QCM controller and HZ-3000 polarization system. The gold-coated electrode of the crystals (6 MHz, 13 mm diameter) was purchased from Hokuto Denko and used as received as a working electrode.

Transmission Electron Microscopy (TEM). TEM images of Au_n−OT were obtained with a Hitachi HF-2000 microscope. Samples for TEM were prepared by drop-casting 4 mL of a 0.5 mg/mL Au_n−OT solution in CH_2Cl_2 onto standard carbon-coated films on copper grids (600 mesh, from Ohta Giken) and drying them in a vacuum overnight. Size distribution of the metal cores were measured from enlarged TEM images for at least 200 individual particles using the computer program Scion Image Release 4 (Scion Corporation).

Scanning Tunneling Microscopy (STM). STM topographic images of the electrodeposited film on HOPG were taken at a constant current of 0.3−0.5 nA and a bias of 0.1−0.5 V with a Pt/Ir (4:1) tip with a PicoSPM (Molecular Imaging) controlled by a PicoScan (Molecular Imaging) at room temperature in air.

Atomic Force Microscopy (AFM). AFM topographic image of the electrodeposited film on HOPG was obtained with a SiN cantilever with a spring constant of 0.12 N/m (Digital Instruments) in contact mode (6 mm scanner) with a PicoSPM (Molecular Imaging) controlled by a PicoScan (Molecular Imaging) at room temperature in air.

Calculations of Anion Diameter. The anion structures of the electrolyte were optimized by the MM+ method with the default parameters packaged with the computer program, HyperChem Release 6 (HyperCube Ltd).

Results and Discussion

Syntheses. Au_n−OTs were prepared by the Brust method, using the reduction of $HAuCl_4$ with a 10-fold excess of $NaBH_4$ in the presence of octanethiol in a single organic phase.[1a] The average core diameter of Au_n−OT thus prepared was determined by TEM to be 2.3 ± 0.5 nm. This core size corresponds to 309 Au atoms, a magic number of cuboctahedron core shape, and an average of 92 octyl thiolate units are bound to the surface of one particle.[24]

The number of exchanged BFcS on the Au_n−OT surface θ_{BFc} was calculated by the ratio of the integrals of the ^{1}H NMR signals between BFc and methyl protons at 3.9−4.7 and 0.8−0.9 ppm, respectively. The reaction condition of i, ii, and iii noted in the Experimental Section produced three types of Au_n−BFc with θ_{BFc} = 3.6, 7.5, and 15, respectively, indicating that the more concentrated solution and longer reaction time produced Au_n−BFc with a larger θ_{BFc}. The UV−vis spectrum of Au_n−BFc in CH_2Cl_2 exhibited a surface plasmon band[25] at 516 nm (ϵ_{max} = 7.7 × 10^5 M^{-1} cm^{-1}).

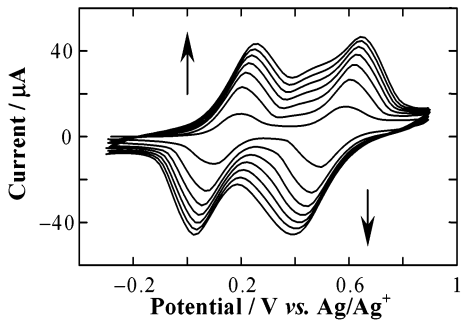

Figure 2. Cyclic voltammograms of 5.0 μM Au_n−BFc (θ_{BFc} = 15) at HOPG in 0.1 M Bu_4NClO_4−CH_2Cl_2 at 100 mV/s between −0.3 to 0.9 V vs Ag/Ag$^+$ in the positive direction from bottom to the top with the first, 10th, 20th, 30th, 40th, 50th, and 60th cyclic scans.

Electrodeposition Behavior of Au_n−BFc (θ_{BFc} = 15): Dependence of the Electrolyte Species in a Solution. Three electrolyte salts of a tetra-*n*-butylammonium cation (Bu_4N^+) with three respective different anions, ClO_4^-, BF_4^-, and PF^-, were employed in order to examine the effects of the counterion on the deposition process of Au_n−BFc (θ_{BFc} = 15). Figure 2 shows the typical cyclic voltammograms of Au_n−BFc in the electrodeposition process, which is measured in a solution of Au_n−BFc at HOPG in Bu_4NClO_4−CH_2Cl_2. The peak current increases gradually by consecutive potential scans between −0.3 and 0.9 V vs Ag/Ag$^+$, where a two-step one-electron oxidation due to BFc units on a particle surface occurs at 0.15 and 0.54 V vs Ag/Ag$^+$. The peak-to-peak separation slowly becomes larger with increasing the number of cyclic scans since the higher film resistance prevents the electron transfer in a thicker film. Cyclic voltammogram of the electrode film thus prepared exhibited two of each cathodic and anodic waves, the peak currents of which were proportional to the potential scan rate in pure Bu_4NClO_4−CH_2Cl_2 indicating the behavior of surface immobilized redox species. It should be noted that there appear additional anodic and cathodic shoulders at ca. 0.3 V between the major waves. This can be ascribed to the chemical decomposition of the biferrocenium unit in the electrodeposited film as observed for the SAM of BFcS on an Au(111) surface.[19c]

We also observed the current growth in cyclic voltammograms when the other electrolytes, Bu_4NBF_4 and Bu_4NPF_6, were adopted; however, its increasing rate depends on the anion, as shown in Figure 3A, which displays the cyclic voltammograms at the 60th potential cycle in Au_n−BFc solution with each electrolyte. The peak currents measured in ClO_4^- and BF_4^- containing solution are comparable, whereas in PF_6^- solution the current is reduced to almost half that of the others. A similar electrolyte effect is detectable in the UV−vis spectra of the Au_n−BFc films on ITO (Figure 3B). The films formed in the ClO_4^- and BF_4^- solutions exhibit similar intensity and maximal absorbance at ca. 550 nm, which is derived from the red-shifted surface plasmon band of closely assembled Au_n−BFcs in the film.[2h,26] In contrast, the film prepared in the PF_6^- solution is about one-fourth that of the others in absorbance intensity. The color change in photos of the Au_n−BFc films by changing the number of cyclic potential scans evidently confirm this difference of the electrodeposition rate, as displayed in Figure 4. These results deduce that the electrodeposition rate of Au_n−BFc in PF_6^- solution is inhibited compared to that in ClO_4^- or BF_4^- solution.

There are two possible factors to cause the effects of the electrolyte anion. The first is the difference in the "redox

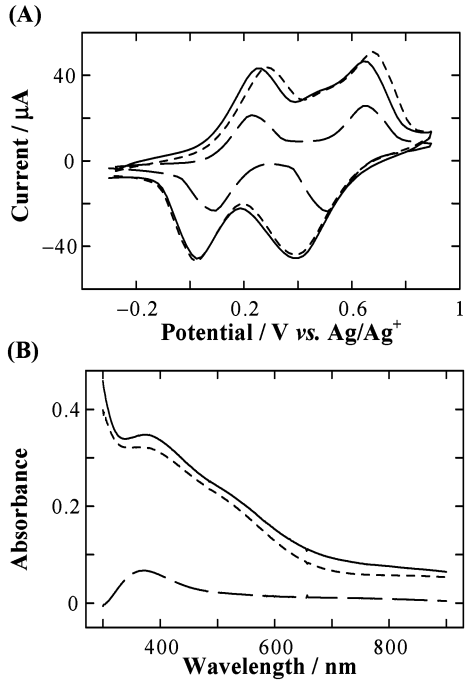

Figure 3. (A) Cyclic voltammograms of 5.0 μM Au_n−BFc (θ_{BFc} = 15) at HOPG in 0.1 M Bu_4NClO_4−CH_2Cl_2 (solid), Bu_4NBF_4−CH_2Cl_2 (dotted), and Bu_4NPF_6−CH_2Cl_2 (dashed) at 100 mV/s between −0.3 and 0.9 V vs Ag/Ag^+ in the positive direction at the 60th cyclic potential scan. (B) UV−vis spectra of electrodeposited Au nanoparticle films prepared in a solution of 5.0 μM Au_n−BFc (θ_{BFc} = 15) in 0.1 M Bu_4NClO_4−CH_2Cl_2 (solid line), Bu_4NBF_4−CH_2Cl_2 (dotted line), and Bu_4NPF_6−CH_2Cl_2 (dashed line) at ITO at 100 mV/s between −0.3 and 0.9 V vs Ag/Ag^+ with 60 scans.

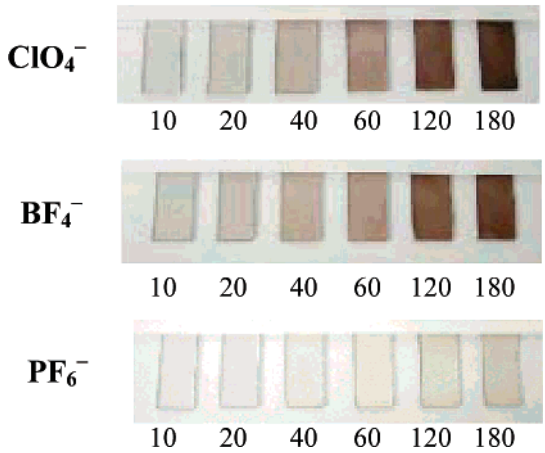

Figure 4. Photographs of electrodeposited Au nanoparticle films prepared in a solution of 5.0 μM Au_n−BFc (θ_{BFc} = 15) at ITO in CH_2Cl_2 with 0.1 M tetra-*n*-butylammonium salt of anion given in the figure at ITO at 100 mV/s between −0.3 and 0.9 V vs Ag/Ag^+. The values in the figure are those of the cyclic scans.

TABLE 1: Redox Potential of Au_n−BFc (θ_{BFc}= 15) and Electrolyte Anion Diameters

electrolyte	$E^{0\prime}{}_1$/V[a]	$E^{0\prime}{}_2$/V[a]	anion diameter/Å
Bu_4NClO_4[b]	0.15	0.54	2.3
Bu_4NBF_4[b]	0.15	0.54	2.1
Bu_4NPF_6[b]	0.17	0.59	3.3

[a] Potential refer to Ag/Ag^+. [b] In 0.1 M electrolyte−CH_2Cl_2 at HOPG.

potential of Au_n−BFc" depending on the electrolyte anion (see Table 1). In Bu_4NPF_6−CH_2Cl_2, the second redox potential $E^{0\prime}{}_2$ is more positive than the second redox potentials in the other two electrolytes by 50 mV, resulting in a decrease of the period during which the biferrocene units are held in the 2+ state when the potential range is fixed as between −0.3 and 0.9 V.[26] However, in a complementary experiment in which the potential range of the cyclic potential scan in PF_6^- solution was shifted in the more positive direction by 50 mV (namely, scanned between −0.25 and 0.95 V), the redox activity in the film that formed was not still comparable to the redox activities in the solutions of the other two anions.

The second factor is the "anion size effect". Presumably, anions surround the biferrocenium units on the Au_n−BFc surface as a counterion in the electrooxidation process. The charged Au_n−BFcs and the counteranions are likely to assemble voluntarily as a result of their lattice energy involving electrostatic force and van der Waals-like force. Hence, when the particles can get closer to each other with the smaller anions, the electrodeposition proceeds efficiently with a larger attractive van der Waals-like force, which prevents the dissolution of the deposited particles on rereduction to the neutral biferrocene state. The diameter of PF_6^-, 3.3 Å, is prominently larger than that of the other anions (ClO_4^-, 2.3 Å; BF_4^-, 2.1 Å), as shown in Table 1, which accords well with the experimental results described above. This anion effect is a convincing proof of the importance of interparticle electrostatic interaction in this electrodeposition mechanism.

STM Images of the Electrodeposited Au_n−BFc Films: Dependence of the Number of Potential Scans and Basic Morphological Aspects. We investigated the morphological features of the Au_n−BFc film and the changes in the surface structure by increasing the number of potential scans in the electrodeposition process. STM images of the Au_n−BFc (θ_{BFc} = 3.6) films at HOPG deposited in ClO_4^- solution by 5 and 60 cyclic scans are shown in Figure 5. Figure 5A shows that the spherical Au_n−BFcs gather to construct an island of particles, but the whole electrode area is not covered and the clear step line of the HOPG surface still appears when the number of potential scans is five. Figure 5B shows that, by 60 potential scans, the Au_n−BFcs of a similar size are tightly assembled to cover all the electrode and build up multiple layers with a fairly flat surface.

Figure 5C is the enlarged image of Figure 5B, and shows that the average spacing between the adjoining electrodeposited Au_n−BFcs is 7.5 nm. This value is obviously larger than the estimated maximal Au_n−BFc particle size of 5.9 nm (core diameter, 2.3 nm; octyl thiolate, 1.0 nm; and biferrocene, 0.8 nm) even if a deviation in core diameter of 0.5 nm is taken into consideration. This finding implies that the Au_n−BFcs are not electrodeposited via direct contact between BFc moieties and/or the alkyl chain, but are electrodeposited by maintaining a certain distance between the particles. At this stage we can exclude the possibility of the deposition mechanism involving a "chemical combination" between adjacent Au_n−BFcs with oxidized BFc units. We have checked the morphology of the Au_n−BFc films on the other electrolytes Bu_4NBF_4 and Bu_4NPF_6 used for electrodeposition, and the STM images confirmed that the average interparticle distance is independent of electrolyte, maintained at 7.5 nm in all cases. The coverage of the Au_n−BFc monolayer Γ_{mono} is calculated as 3.2×10^{-12} mol cm^{-2}.[13] It should be mentioned that our previous report on the Au_n−AQ with an estimated maximal diameter of 5.8 nm[2h] has shown that the inter-nanoparticle distance in the Au_n−AQ film electrodeposited in Bu_4NClO_4−CH_2Cl_2 was 8.5 nm, indicating an existence of spacing between the Au_n−AQs as the same feature as Au_n−BFcs.

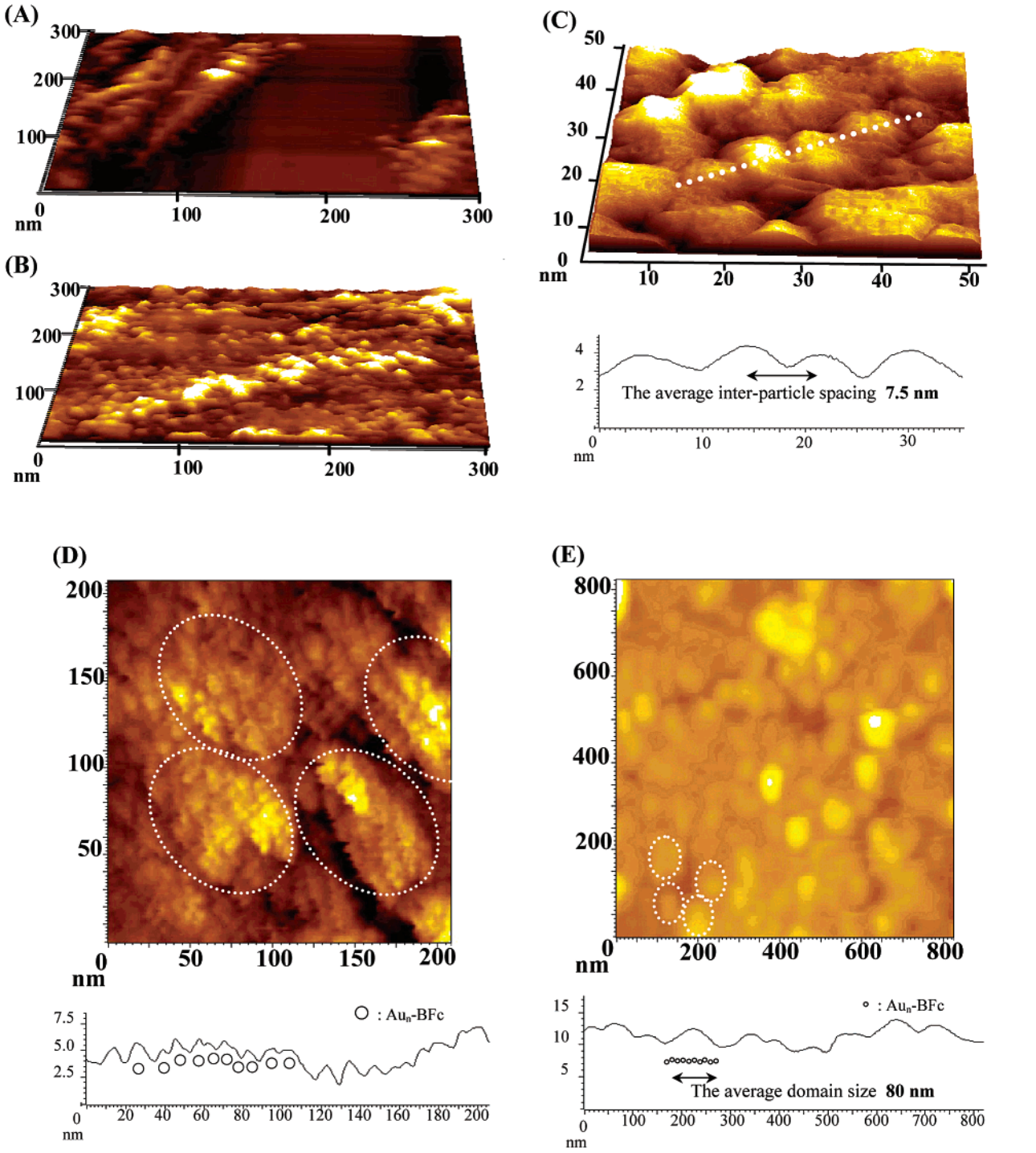

Figure 5. The STM image of the Au_n−BFc ($\theta_{BFc} = 3.6$) film on HOPG electrodeposited in 5.3 μM Au_n−BFc ($\theta_{BFc} = 3.6$) in 0.1 M Bu_4NClO_4−CH_2Cl_2 between −0.3 and 0.9 V vs Ag/Ag^+ at 100 mV/s by 5 (A) and 60 (B) cyclic potential scans. (C) The enlarged STM image of Figure 5B (top), and the cross-sectional profile along the dotted line (bottom). The STM (D, top) and AFM (E, top) images of the Au_n−BFc ($\theta_{BFc} = 7.5$) film on HOPG electrodeposited in 5.2 μM Au_n−BFc ($\theta_{BFc} = 7.5$) in 0.1 M Bu_4NClO_4−CH_2Cl_2 between −0.3 and 0.9 V vs Ag/Ag^+ at 100 mV/s by 5 cyclic scans, and the typical cross-sectional profile along the cross axis (bottom).

The most likely candidate for the chemical species existing in the space among adjacent Au_n−BFcs in the film, estimated at 7.5−5.9 = 1.6 nm (Figure 6), is the used electrolyte, even if the potential in the electrodeposition experiment is stopped at −0.3 V where BFc units are in the neutral state. It is a matter of interpretation that not all of the anions which gather around the oxidized BFc units as counterions in the electrodeposition process are removed; some of them are immobilized into the interparticle space of the film even after the potential is set back to −0.3 V.

The presence of anions and the proportion of Au_n−BFc particles and BF_4^- anions in the film prepared in BF_4^- solution were examined by PGA and ICP. The boron content of the film assayed by PGA after subtracting the contribution from the HOPG substrate (0.30 ppm) was determined as 8.9×10^{-8} mol (2.9×10^{-8} mol cm^{-2}). The concentration of the gold contained in the film was determined as 1.08 ppm with ICP. Considering the average molecular weight of one nanoparticle (Au_{309} = 60862), the amount of the deposited Au_n−BFc ($\theta_{BFc} = 7.5$) was quantified as 8.9×10^{-10} mol (3.2×10^{-10} mol cm^{-2}),

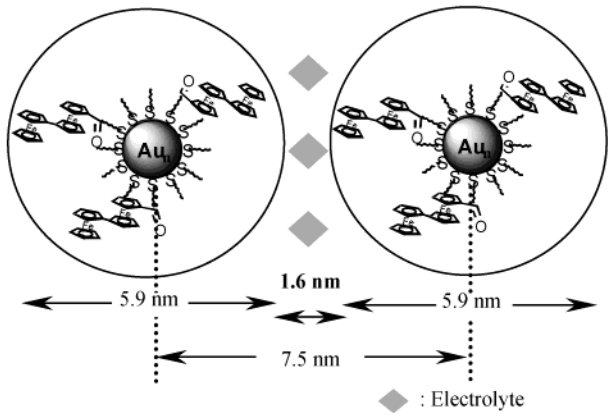

Figure 6. The illustration of adjacent electrodeposited Au$_n$−BFcs in the film.

which gave the ratio of the Au$_n$−BFc ($\theta_{BFc} = 7.5$) particle and BF_4^- anion in the film as 1:9.3. This value is suitable for the estimation that 62% of the counteranions of BFc^{2+} remain as spacers.

STM and AFM Images of the Electrodeposited Au$_n$−BFc Films: Dependence of the Modification Number of BFc Sites on the Particle Surface and Specific Film Structure. STM and AFM images of the Au$_n$−BFc film with a larger modification number ($\theta_{BFc} = 7.5$) are shown in Figure 5D,E. In contrast to the image for Au$_n$−BFc ($\theta_{BFc} = 3.6$) shown in Figure 5A, the Au$_n$−BFcs ($\theta_{BFc} = 7.5$) completely concealed the electrode surface to form the particle film which is flat within a level of 5 nm in height in the same electrolysis conditions as displayed in Figure 5D. In the UV−vis spectra, the absorbance of the Au$_n$−BFc ($\theta_{BFc} = 7.5$) film was 3 times larger than that of the Au$_n$−BFc ($\theta_{BFc} = 3.6$) film, suggesting that the electrodeposition rate is faster for Au$_n$−BFcs with higher θ_{BFc}. Notably, a thicker Au$_n$−BFc film can be constructed by increasing the number of potential scans even in a solution of Au$_n$−BFc ($\theta_{BFc} = 3.9$), and the surface morphology (i.e., interparticle distance) is independent of the θ_{BFc} value.

The surface in Figure 5D maintains a monolayer-level flatness seen in its cross sectional view, whereas it is apparent that domains of particles ca. 70−80 nm in diameter (encircled by a dotted line) are constructed. The AFM image of the same sample shown in Figure 5E reveals the peculiar nanostructure of the Au$_n$−BFc film; round-shaped domains spreading on the whole surface as if huge particles are assembled on the electrode. The cross sectional profile demonstrates that the domain size is fairly uniform, with an average diameter of ca. 80 nm, corresponding to ca. 100 Au$_n$−BFc particles assuming that Au$_n$−BFcs are packed with a spacing of 7.5 nm.

EQCM Measurement of Au$_n$−BFc Deposition. EQCM measurement was carried out to analyze the mass change in the electrochemical process. Figure 7 displays the typical EQCM behavior of Au$_n$−BFc ($\theta_{BFc} = 7.5$) at a gold electrode in Bu_4NClO_4−CH_2Cl_2. In the first potential sweep in the positive direction, only a slight frequency decrease is observed in the first electron oxidation of the BFc moieties at $E^{0\prime}_1 = 0.15$ V, whereas the frequency decreases dramatically from 0.54 to 0.9 V when the second electron oxidation of the BFc sites takes place at $E^{0\prime}_2 = 0.54$ V. This behavior reflects that the electrooxidative aggregation of Au$_n$−BFcs occurs by the two-electron oxidation of the BFc units, since a frequency decrease relates to a mass increase on the electrode. When the potential scan was reversed at 0.9 V to the negative potential, the frequency continues to decrease until 0.54 V; however, a

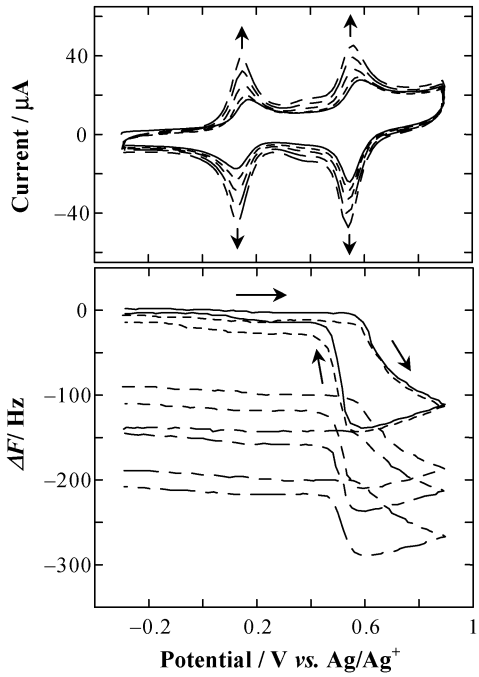

Figure 7. Cyclic voltammograms (top) and ΔF-potential curves (bottom) of 5.2 μM Au$_n$−BFc ($\theta_{BFc} = 7.5$) at a gold electrode in 0.1 M Bu_4NClO_4−CH_2Cl_2 at 100 mV/s between −0.3 and 0.9 V vs Ag/Ag^+ in the positive direction with the first (solid line), fifth (dotted line), 10th (dashed line), 15th (dotted−dashed line), and 20th (2-dotted−dashed line) scans.

significant frequency increase starts after the electrode potential becomes more negative than $E^{0\prime}_2$. Thus, the frequency difference before and after the potential cycling at −0.3 V corresponds to the net weight of the deposited Au$_n$−BFcs. For example, a frequency decrease of 6.0 Hz after the first scan corresponds to 9.7×10^{-8} g increase in mass weight calculated by the Sauerbery equation of $\Delta F = -C\Delta W$, where ΔF is the frequency change, C is the proportional constant that depends on the parameters of QCM electrode properties (e.g., the electrode area, quartz density, and quartz elasticity, and the value is equivalent to 6.17×10^7 Hz g^{-1} in this study), and ΔW is the weight change on the electrode. During the course of repeated cyclic potential scans, similar ΔF-potential behavior in one cycle was observed, and the frequency steadily decreased after each cycle with current increase of cyclic voltammograms, indicating that the Au$_n$−BFc layer is continuously accumulated on the electrode surface. These EQCM results are interpretable as follows: (1) Au$_n$−BFcs are apt to aggregate at the electrode/electrolyte interface and adsorb to the electrode by the formation of the BFc^{2+} state on the particle surface, (2) significant desorption of assembled Au$_n$−BFcs from the electrode occurs after BFc sites are returned to the neutral state by reduction, and (3) a small portion of the strongly adsorbed flocks of Au$_n$−BFcs remain on the electrode. By repeating the potential scans, the Au$_n$−BFc film might be fabricated by the remaining adsorbed Au$_n$−BFcs, resulting in the formation of the domains demonstrated in the STM and AFM images (Figure 8, in the i, ii, and iii processes).

EQCM Measurement of the Au$_n$−BFc Film. EQCM measurement of the Au$_n$−BFc film was carried out to gain insight on the movement of electrolyte ions in the redox process of the film. Figure 9, top, shows the cyclic voltammogram of the Au$_n$−BFc ($\theta_{BFc} = 7.5$) film (prepared in PF_6^- solution) for 2 scans, showing a stable two-step one-electron redox wave of BFc moieties. The coverage of the Au$_n$−BFc in this film Γ_{BFc}

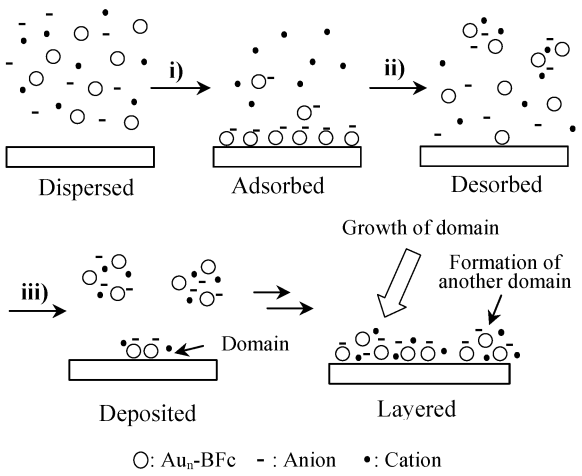

Figure 8. The illustration of the electrodeposition process in Au_n−BFc solution at the electrode interface. (i) Two-electron oxidation of the BFc sites, (ii) set back to the neutral state by two-electron reduction, and (iii) repeating the potential sweep.

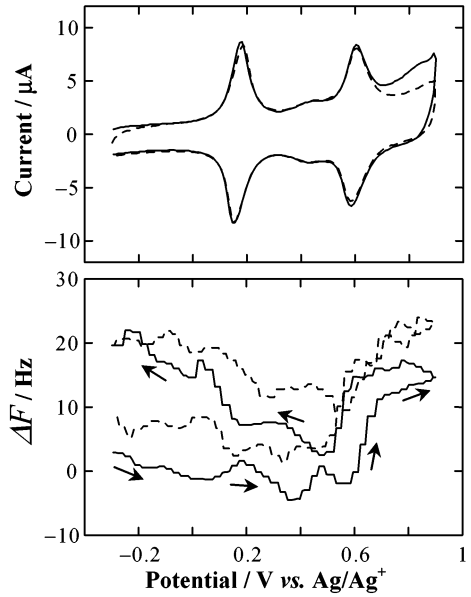

Figure 9. Cyclic voltammograms (top) and ΔF-potential curves (bottom) of a Au_n−BFc ($\theta_{BFc} = 7.5$) film on a gold electrode in 0.1 M Bu_4NPF_6−CH_2Cl_2 at 30 mV/s between −0.3 to 0.9 V vs Ag/Ag^+ in the positive direction with the first (solid) and second (dotted) scan. The film was prepared in a 5.2 μM Au_n−BFc ($\theta_{BFc} = 7.5$) in 0.1 M Bu_4NPF_6−CH_2Cl_2 at 100 mV/s between −0.3 and 0.9 V vs Ag/Ag^+ in the positive direction with 25 scans.

is calculated as 2.1×10^{-11} mol cm^{-2} with 6.7 particle layers. It is possible to estimate the total weight of the Au_n−BFc film ΔW_{CV} by the following equation:

$$\Delta W_{CV} = Q(W_{Au} + 9.3W_{elec})/F\theta_{BFc} \quad (1)$$

where Q (C) is the redox charge calculated by the first peak current in Figure 9, top; W_{Au} and W_{elec} are the molecular weight of Au_n−BFc ($\theta_{BFc} = 7.5$) and the Bu_4NPF_6 electrolyte, respectively, in g mol^{-1}; and F is the Faraday constant (96500 C mol^{-1}), supposing that the rate of the simultaneously deposited electrolyte is the same as that in the case in Bu_4NBF_4−CH_2Cl_2 (vide supra). The value of ΔW_{CV} is calculated as 2.4×10^{-6} g, which is reasonable compared to the amount estimated based on the frequency change in the electrodeposition process ΔW_{QCM}, determined as 3.6×10^{-6} g with the frequency decrease in 221 Hz. The discrepancy between the two values might be caused by factors such as the frequency change generated by the viscoelasticity of the film, solvent molecules included in the film, and/or Au_n−BFcs removed by rinsing with CH_2Cl_2 after the deposition.

The ΔF-potential curves of the film in Figure 9, bottom, reveal that the frequency decreases until the potential reaches ca. 0.5 V; conversely, the frequency starts to increase significantly after ca. 0.6 V, around $E^{0\prime}{}_2$ of BFc units. The tendency of frequency change in one potential cycle is considerably similar, suggesting that some chemical species are excluded from the film reversibly at the potential more positive than $E^{0\prime}{}_2$. The ΔF decrease at $E^{0\prime}{}_1$ is elucidated by the entry of the anions inside the Au_n−BFc film to fill the spaces among the particles by one-electron oxidation of BFc units. As for the ΔF increase at $E^{0\prime}{}_2$, the first plausible interpretation is that the second redox reaction is accompanied not by the introduction of the anion species, but by the release of the cation species from the film. This assumption is valid in a situation that the electrolyte was included in advance before the oxidation reaction; namely, the cations should be simultaneously involved as a counterion to detected anions in the film as described in the PGA and ICP experiment even when the BFc is in the neutral form. Presuming that all the cations (Bu_4N^+) in the film corresponding to 50% of the number of BFc sites come out at $E^{0\prime}{}_2$, the decrease of weight in the film equals 2.6×10^{-8} g, whereas the amount determined by a frequency increase of 10 Hz, shown in Figure 9, bottom, corresponds to 1.6×10^{-7} g, of which value is ca. 6 times larger of the estimated value. This discrepancy proves that not only the included cations of electrolyte, but also other chemical species in the film should be considered to explain the ΔF increase at $E^{0\prime}{}_2$. The desorption of Au_n−BFc in some parts of the film is hardly practicable, since the Au_n−BFc particles are positively tend to increase the attractive interaction over $E^{0\prime}{}_2$ (vide supra) and the cyclic voltammograms in Figure 9, top, exhibit stable current waves. Thus, that the rational elucidation is "the exclusion of solvent molecules". The second oxidation of the BFc moieties in the Au_n−BFc film provokes an increase in the local ionic interaction with the anions and gains the polarity around the particles; subsequently, the less-polar solvent molecules of CH_2Cl_2 are naturally expelled from the charged Au_n−BFc film. The decrease of 1.3×10^{-7} g (=1.6×10^{-7} g − 2.6×10^{-8} g) is equivalent to the loss of 54 molecules per Au_n−BFc particle. This value is adequate judging from the size of the interparticle space.

A simplified picture of chemical species motion for the two-step redox reaction of Au_n−BFc in the film is shown in Figure 10. We expect that the porous Au_n−BFc film with long interparticle spacing acts like a nano-sponge and the solvent molecules, anions in the solution, and possibly cations pre-included move into and out from the film reversibly at $E^{0\prime}{}_2$ by changing the electronic charge of the BFc sites (Figure 10, ii). Additionally the exclusion of solvent is not observed at $E^{0\prime}{}_1$ in accordance with the electrodeposition phenomenon of Au_n−BFcs. It is inferred that exclusion of solvent molecules around Au_n−BFcs at $E^{0\prime}{}_2$ causes interparticle approaching and precipitation effectively to form ionic lattice ionic lattice including Au_n−BFc^{2+} and counterion.

We should note that it is still desirable to explain clearly why the interparticle interaction remains when the BFc^{2+} sites are reduced to become the neutral species. In the present stage, it is postulated that the Au_n core also might be positively charged during the deposition process, which causes the attractive interaction among assembled particles and layered films involving electrolyte species even when the potential was set back to

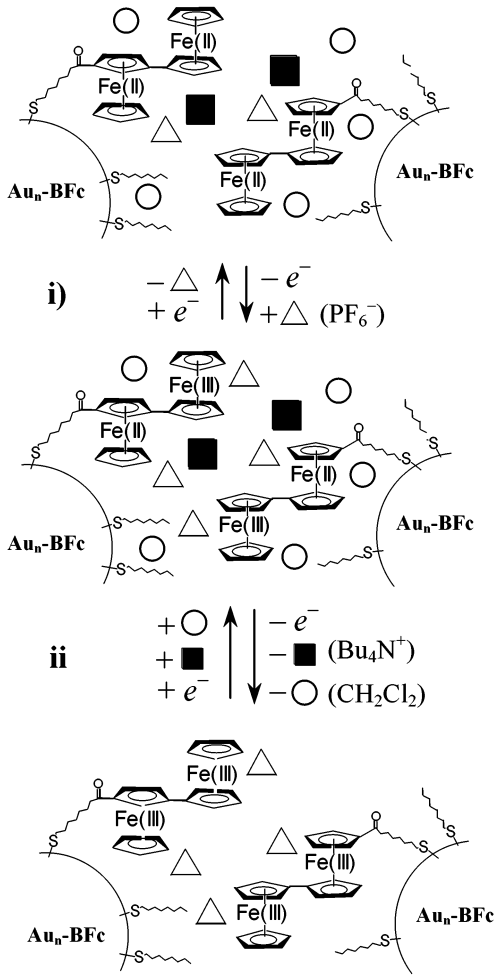

Figure 10. The illustration of ion motion for the two-step redox reaction of Au_n−BFc in the film. The first (i) and the second (ii) redox reaction of the BFc sites in the film.

where BFc sites are in the neutral form. Investigation to clarify this point is currently underway in our laboratory.

Conclusion

The electrodeposition behavior of the biferrocene (BFc)-functionalized Au nanoparticle with a 2.3 ± 0.5 nm core diameter (Au_n−BFc) depends on the number of potential scans, the modification number of BFc units on a Au_n−BFc surface θ_{BFc}, and the electrolyte in solution. The average interparticle distance of the neighboring Au_n−BFcs in the film is 7.5 nm, which distance is independent of the electrolyte used and longer than the estimated diameter of 5.9 nm. Electrolyte salt exists in the interparticle spaces in the film like a glue to bind the nanoparticles. The electrodeposition of Au_n−BFcs forms circular domains ca. 80 nm in diameter and composed of assembled nanoparticles. Mass change at the electrode surface in the electrodeposition process clarified that the interaction between the Au_n−BFc^{2+} particles would be intensified by the exclusion of solvent molecules among the charged particles.

Acknowledgment. This work was supported by Grants-in-Aid for Scientific Research (No. 14204066) from the Ministry of Culture, Education, Science, Sports, and Technology, Japan, and the Research Fellowships of the Japan Society for the Promotion of Science for Young Scientists.

Supporting Information Available: The TEM image and the core diameter histogram of Au_n−BFc (Figure S1), ^{1}H NMR signals of Au_n−BFc in $CDCl_3$ (Figure S2), and the STM images of the biferrocene-attached Pd nanoparticles (θ_{BFc} = 26.3) film on HOPG electrodeposited in CH_2Cl_2 with 0.1 M Bu_4NClO_4 (Figure S3). This material is available free of charge via the Internet at http://pubs.acs.org.

References and Notes

(1) (a) Brust, M.; Walker, M.; Bethell, D.; Schiffrin, D. J.; Whyman, R. *J. Chem. Soc., Chem. Commun.* **1994**, 801. (b) Ziegler, K. J.; Doty, R. C.; Johnston, K. P.; Korgel, B. A. *J. Am. Chem. Soc.* **2000**, *123*, 7797. (c) Wu, M. L.; O'Neill, S. A.; Brousseau, L. C.; McConnell, W. P.; Shultz, D. A.; Linderman, R. J.; Feldheim, D. L. *J. Chem. Soc., Chem. Commun.* **2000**, 775. (d) Chen, S. W.; Truax, L. A.; Sommers, J. M. *Chem. Mater.* **2000**, *12*, 3864. (e) Templeton, A. C.; Wuelfing, M. P.; Murray, R. W. *Acc. Chem. Res.* **2000**, *33*, 27. (f) Pan, C.; Pelzer, K.; Philippot, K.; Chaudret, B.; Dassenoy, F.; Lecante, P.; Casanove, M. J. *J. Am. Chem. Soc.* **2001**, *123*, 7584.

(2) (a) Chen, S. W.; Murray, R. W.; Feldberg, S. W. *J. Phys. Chem. B* **1998**, *102*, 9898. (b) Chen, S. W.; Ingram, R. S.; Hostetler, M. J.; Pietron, J. J.; Murray, R. W.; Schaaff, T. G.; Khoury, J. T.; Alvarez, M. M.; Whetten, R. L. *Science* 1**998**, *280*, 2098. (c) Korgel, B. A.; Fullam, S.; Connolly, S.; Fitzmaurice, D. *J. Phys. Chem. B* **1998**, *102*, 8379. (d) Maye, M. M.; Lou, Y. B.; Zhong, C. J. *Langmuir* **2000**, *16*, 7520. (e) Hicks, J. F.; Zamborini, F. P.; Osisek, A.; Murray, R. W. *J. Am. Chem. Soc.* **2001**, *123*, 7048. (f) Haram, S. K.; Quinn, B. M.; Bard, A. J. *J. Am. Chem. Soc.* **2001**, *123*, 8860. (g) Shipway, A. N.; Willner, I. *J. Chem. Soc., Chem. Commun.* **2001**, 2035. (h) Yamada, M.; Tadera, T.; Kubo, K.; Nishihara, H. *Langmuir* **2001**, *17*, 2363.

(3) Cantele, G.; Ninno, D.; Iadonisi, G. *Phys. Rev. B* **2000**, *61*, 13730.

(4) (a) Hroves, J. T.; Ulman, N.; Boxer, S. G. *Science* **1997**, *275*, 651. (b) Wang, B.; Wang, H. Q.; Li, H. X.; Zeng, C. G.; Hou, J. G.; Xiao, X. D. *Phys. Rev. B* **2001**, *6303*, 5403.

(5) Novak, J. P.; Brousseau, L. C.; Vance, F. W.; Johnson, R. C.; Lemon, B. I.; Hupp, J. T.; Feldheim, D. L. *J. Am. Chem. Soc.* **2000**, *122*, 12029.

(6) (a) Kiely, C. J.; Fink, J.; Brust, M.; Bethell, D.; Schiffrin, D. J. *Nature* **1998**, *396*, 444. (b) Sun, S. H.; Murray, C. B.; Weller, D.; Folks, L.; Moser, A. *Science* **2000**, *287*, 1989. (c) Jin, J.; Iyoda, T.; Cao, C. S.; Song, Y. L.; Jiang, L.; Li, T. J.; Ben Zhu, D. *Angew. Chem., Int. Ed.* **2001**, *40*, 2135.

(7) (a) Gittins, D. I.; Bethell, D.; Nichols, R. J.; Schiffrin, D. J. *J. Mater. Chem.* **2000**, *10*, 79. (b) Men, Y.; Kubo, K.; Kurihara, M.; Nishihara, H. *Phys. Chem. Chem. Phys.* **2001**, *3*, 3377.

(8) (a) Caruso, F.; Mohwald, H. *Langmuir* **1999**, *15*, 8276. (b) Pardo-Yissar, V.; Katz, E.; Lioubashevski, O.; Willner, I. *Langmuir* **2001**, *17*, 1110. (c) Caruso, F.; Spasova, M.; Saigueirino-Maceira, V.; Liz-Marzan, L. M. *Adv. Mater.* **2001**, *13*, 1090.

(9) (a) Zamborini, F. P.; Hicks, J. F.; Murray, R. W. *J. Am. Chem. Soc.* **2000**, *122*, 4514. (b) Templeton, A. C.; Zamborini, F. P.; Wuelfing, W. P.; Murray, R. W. *Langmuir* **2000**, *16*, 6682.

(10) (a) Taton, T. A.; Mucic, R. C.; Mirkin, C. A.; Letsinger, R. L. *J. Am. Chem. Soc.* **2000**, *122*, 6305. (b) Musick, M. D.; Keating, C. D.; Lyon, L. A.; Botsko, S. L.; Pena, D. J.; Holliway, W. D.; McEvoy, T. M.; Richardson, J. N.; Natan, M. J. *Chem. Mater.* **2000**, *12*, 2869. (c) McConnell, W. P.; Novak, J. P.; Brousseau, L. C.; Fuierer, R. R.; Tenent, R. C.; Feldheim, D. L. *J. Phys. Chem. B* **2000**, *104*, 8925.

(11) Gittins, D. I.; Bethell, D.; Schiffrin, D. J.; Nichols, R. J. *Nature* **2000**, *408*, 6808.

(12) (a) Lahav, M.; Heleg-Shabtai, V.; Wasserman, J.; Katz, E.; Willner, I.; Durr, H.; Hu, Y. Z.; Bossmann, S. H. *J. Am. Chem. Soc.* **2000**, *122*, 11480. (b) Yamada, M.; Kuzume, A.; Kurihara, M.; Kubo, K.; Nishihara, H. *J. Chem. Soc., Chem. Commun.* **2001**, 2476.

(13) Horikoshi, T.; Itoh, M.; Kurihara, M.; Kubo, K.; Nishihara, H. *J. Electroanal. Chem.* **1999**, *473*, 113.

(14) (a) Yamada, M.; Quiros, I.; Mizutani, J.; Kubo, K.; Nishihara, H. *Phys. Chem. Chem. Phys.* **2001**, *3*, 3377. (b) Quiros, I.; Yamada, M.; Mizutani, J.; Kubo, K.; Kurihara, M.; Nishihara, H. *Langmuir* **2002**, *18*, 1413. (c) Yamada, M.; Nisihara, H. *J. Chem. Soc., Chem. Commun.* **2002**, 2578.

(15) (a) Ingram, R. S.; Hostetler, M. J.; Murray, R. W. *J. Am. Chem. Soc.* **1997**, *119*, 9175. (b) Templeton, A. C.; Cliffel, D. E.; Murray, R. W. *J. Am. Chem. Soc.* **1997**, *121*, 77081.

(16) (a) Yamada, M.; Kubo, K.; Nishihara, H. *Chem. Lett.* **1999**, 1335. (b) Nishiyama, K.; Kubo, A.; Taniguchi, I.; Yamada, M.; Nishihara, H. *Electrochemistry* **2001**, *69*, 980. (c) Murata, M.; Yamada, M.; Fujita, T.; Kojima, K.; Kurihara, M.; Kubo, K.; Kobayashi, Y.; Nishihara, H. *J. Am. Chem. Soc.* **2001**, *123*, 12903.

(17) (a) Green, S. J.; Stokes, J. J.; Hostetler, M. J.; Pietron, J.; Murray, R. W. *J. Phys. Chem. B* **1997**, *101*, 2663. (b) Labande, A.; Astruc, D. *J. Chem. Soc., Chem. Commun.* **2000**, 1007. (c) Chen, S. W. *Langmuir* **2001**, *17*, 6664.

(18) Larsen, A. E.; Grier, D. G. *Nature* **1997**, *385*, 230.
(19) (a) Mueller-Westerhof, U. T. *Angew. Chem., Int. Ed. Engl.* **1986**, *25*, 5. 702. (b) Astruc, D. *Electron-Transfer and Radical Processes in Transition Metal Chemistry;* VCH: New York, 1995. (c) Kubo, K.; Kondow, H.; Nishihara, H. *Electrochemistry* **1999**, *67*, 1129.
(20) Chidsey, C. E. D.; Bertozzi, C. R.; Putvinski, T. M.; Mujsce, A. M. *J. Am. Chem. Soc.* **1990**, *112*, 4301.
(21) Yonezawa, C.; Eood, A. K. H.; Hoshi, M.; Ito, Y.; Tachikawa, E. *Nucl. Instrum. Methods Phys. Res.* **1993**, *A329*, 207.
(22) Sakai, Y.; Yonezawa, C.; Magara, M.; Sawahata, H.; Ito, Y. *Nucl. Instrum. Methods Phys. Res.* **1994**, *A353*, 699.
(23) Kubo, M. K.; Sakai, Y. *J. Nucl. Radiochem. Sci.* **2000**, *1*, 83.
(24) Hostetler, M. J.; Wingate, J. E.; Zhong, C.-J.; Harris, J. E.; Vochet, R. W.; Clark, M. R.; Londono, D.; Green. S. J.; Stokes, J. J.; Wignall, G. D.; Porter, M. D.; Evans, N. D.; Murray, R. W. *Langmuir* **1998**, *14*, 17.
(25) (a) Alvarez, M. M.; Khoury, J. T.; Schaaff, T. G.; Shafigullin, M. N.; Vezmar, I.; Whetten, R. L. *J. Phys. Chem. B* **1997**, *101*, 3706. (b) Templeton, A. C.; Pietron, J. J.; Murray, R. W. *J. Phys. Chem. B* **2000**, *104*, 564.
(26) Freeman, R. G.; Grabar, K. C.; Allison, K. J.; Bright, R. M.; Davis, J. A.; Guthrie, P.; Hommer, M. B.; Jackson, M. A.; Smith, P. C.; Walter, D. G.; Natan, M. J. *Science* **1995**, *267*, 1629.